Supplementary Material

Topological valley quasi-bound states in the continuum for radiatively accessible robust transport

Minggui Wei[1], Yang Long[2,*], Gui-Geng Liu[3,*], Jianwei Liu[1], Sudheer Manjima[1], Elbert E. M. Chia[1], Baile Zhang[1,4,*]

[1]Division of Physics and Applied Physics, School of Physical and Mathematical Sciences, Nanyang Technological University, Singapore 637371, Singapore.
[2]School of Physics Science and Engineering, Tongji University, Shanghai 200092, China.
[3]Department of Electronic and Information Engineering, School of Engineering, Westlake University, Hangzhou 310030, China.
[4]Centre for Disruptive Photonic Technologies, The Photonics Institute, Nanyang Technological University, Singapore 639798, Singapore.

*Correspondence: longyangphysics@tongji.edu.cn (Yang Long); liuguigeng@westlake.edu.cn (Gui-Geng Liu); blzhang@ntu.edu.sg (Baile Zhang)

Supplementary Note 1. The time-domain terahertz near-field scanning system

Supplementary Figure 1a illustrates the time-domain terahertz near-field scanning system for the measurement of the near-field electric field. The terahertz beam is collimated by a terahertz lens with a focal length of F = 5 cm. We add two terahertz lenses (F = 10 cm and F = 2.5 cm) to focus the collimated beam. The polarization of the incident beam is adjusted to TE polarization, and the electric field is in the xy plane. Supplementary Figures 1b and 1c depict the normalized electric field intensity and phase distributions of the terahertz beam at f = 0.5050 THz, respectively. In Supplementary Fig. 1d, the electric field intensity distribution along y = 0 mm is shown (red line). The fitted beam waist along the x-direction measures approximately 0.5457 mm (black dashed line). Similarly, in Supplementary Fig. 1e, the electric field intensity distribution along x = 0 mm is displayed as the blue line. The fitted electric field intensity distribution is the black dashed line. The fitted beam waist along the y-direction is approximately 0.4262 mm. A terahertz probe is utilized to record the electric field in the scanning area of the samples. The pitch of the sample holder is calibrated by adjusting the heights between the terahertz probe and the four corners of the scanning area of a sample. In calibration, the heights between the terahertz probe and the four corners of the scanning area of a sample are ~0.066 mm (see Fig. 1b in the main text) with a height error within 0.004 mm. The scan region is 4.00 mm × 9.60 mm with an increment of 0.08 mm for the compound VPCs with straight domain walls. The scan region is 9.20 mm × 8.00 mm with an increment of 0.08 mm for the compound VPCs with a Z-bend domain wall. The scan region is 8.00 mm × 8.40 mm with an increment of 0.08 mm for the compound VPC splitter. The terahertz signal is scanned up to 400 ps, which provides a frequency resolution of 0.0025 THz. We also perform zero-padding up to 3276.8 ps in the time domain data to increase the number of frequency points, resulting in smaller intervals.

Figure 1b (main text) shows the experimental configuration of the sample and the terahertz near-field probe, captured by a CCD camera. As illustrated in Supplementary Fig. 2, a circular LED array concentric with the CCD camera is used as an illumination source. The CCD camera records the light scattered from both the sample surface and the terahertz probe, which appear as the bright regions in Fig. 1b (main text). The extensive black regions in Fig. 1b (main text) do not represent any special structural feature of the sample. They correspond to areas of the sample surface where the incident LED light is reflected and does not enter the collection angle of the CCD camera. As a result, these regions appear dark in the recorded image. The contrast in the image is therefore determined by the amount of scattered light collected by the CCD rather than by the physical geometry of the sample itself.

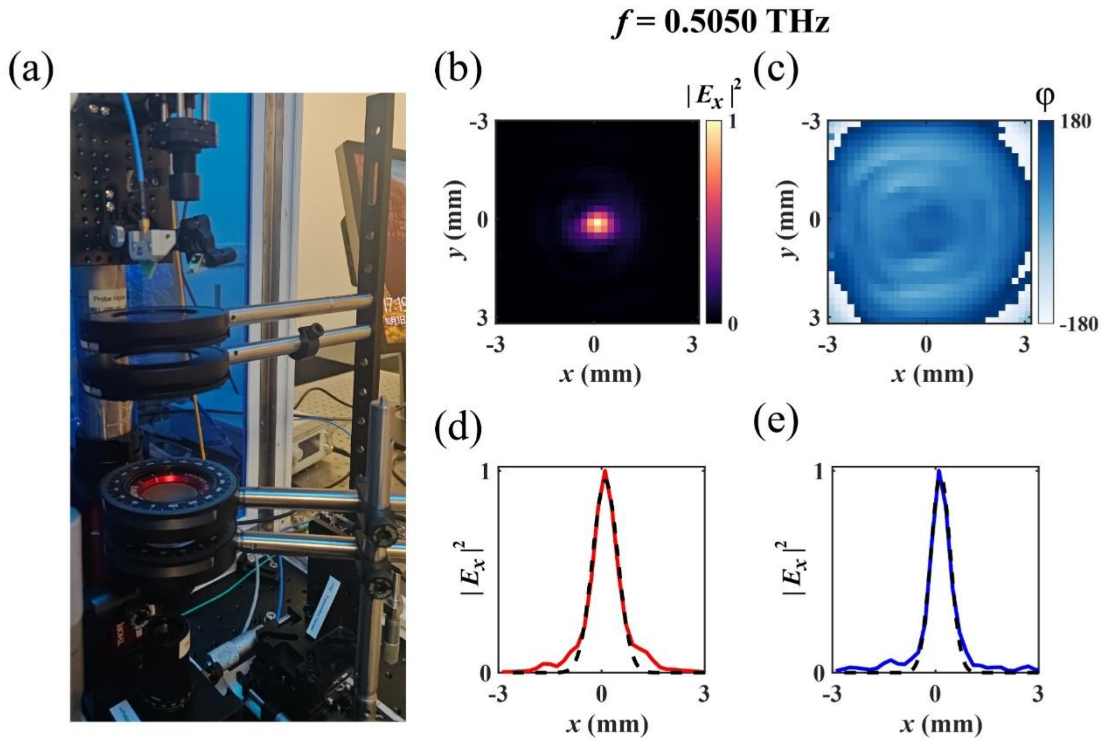

Supplementary Figure 1. The time-domain terahertz near-field scanning system. (a) The time-domain terahertz near-field scanning system for near-field electric-field measurements. (b and c) The normalized electric field intensity distribution and the phase distribution of a terahertz beam at f = 0.5050 THz, respectively. (d) The electric field intensity distribution along y = 0 mm (red line) in (b) and the fitted electric field intensity distribution (black dashed line), respectively. (e) The electric field intensity distribution along x = 0 mm (blue line) in (b) and the fitted electric field intensity distribution (black dashed line), respectively. The electric field intensity distribution is normalized by the maximum value of the electric field intensity distribution.

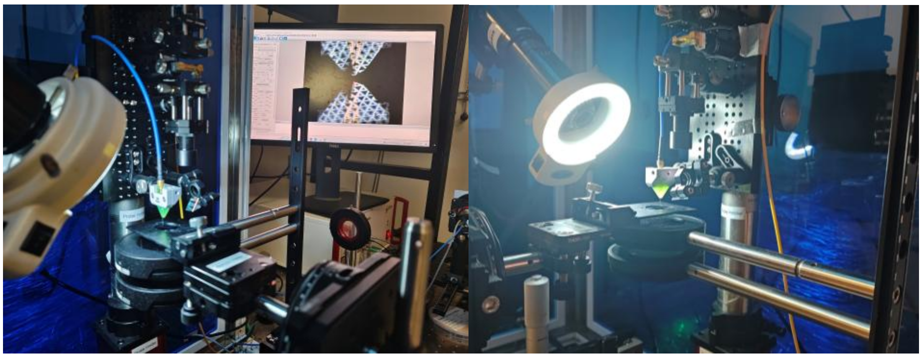

Supplementary Figure 2. The optical images of the experimental setup. (a) The overall view of the experimental setup. (b) The side view of the circular LED array.

Supplementary Note 2. Topological properties of the compound valley photonic crystal (VPC)

The VPC has a honeycomb lattice consisting of two equilateral triangular air holes with side lengths of w_{L1} and w_{D1} (Fig. 2a in the main text), respectively. When the inversion symmetry is preserved ($w_{L1} = w_{D1}$), the VPC has C_6 symmetry, leading to a pair of degenerate Dirac points at K and K′ valleys. Breaking the inversion symmetry ($w_{L1} \neq w_{D1}$) lifts the degeneracy, resulting in the topological band gaps at K and K' valleys. Supplementary Figure 3a illustrates the band structures of VPCs with $w_{L1} = w_{D1}$ and $w_{L1} \neq w_{D1}$, respectively. The black dots and red circles represent the cases with $w_{L1} = w_{D1} = 0.55P/3$ and $w_{L1} = 0.65P/3$, $w_{D1} = 0.45P/3$, respectively. In the VPCs, the Berry curvature is localized around the K and K' valleys with opposite signs, indicating opposite-signed valley Chern numbers that characterize the topological phase of VPCs. Supplementary Figure 3b depicts the corresponding bulk bands of the VPC with $w_{L1} \neq w_{D1}$, where a complete bandgap opens due to inversion-symmetry breaking. When VPCs with different topological phases are combined, topological valley edge states emerge, as shown in Fig. 2c of the main text. A complete bandgap also exists in the compound VPC with $\delta w = 0.12$, as shown in Supplementary Fig. 3c. Similarly, topological valley states emerge at domain walls formed by compound VPCs with different topological phases, giving rise to topological quasi-bound states in the continuum (QBICs).

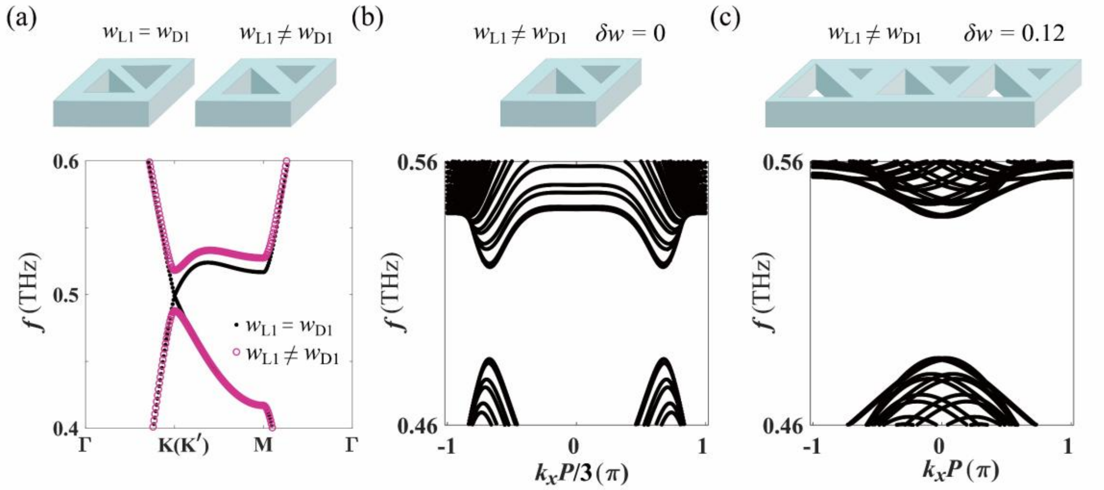

Supplementary Figure 3. The dispersions of the VPCs and a compound VPC. (a) Band structures of the VPCs with $w_{L1} = w_{D1}$ and $w_{L1} \neq w_{D1}$, respectively. The black dots and red circles represent the cases with $w_{L1} = w_{D1} = 0.55P/3$ and $w_{L1} = 0.65P/3$, $w_{D1} = 0.45P/3$, respectively. (b) The corresponding bulk bands of the VPC with $w_{L1} \neq w_{D1}$. (c) The bulk bands of the compound VPC with $\delta w = 0.12$.

Supplementary Note 3. The retrieval of *Q* factors from the propagation lengths

We have fitted the propagation length from near-field measurements by using $|E(x)|^2 \propto \exp(-x/L)$, where x is the coordinate, and L is the intensity propagation length. Then, we retrieved the experimental Q factors. In the following, we perform the propagation length fitting to different samples to retrieve the experimental Q factors at different frequencies, which correspond to different momenta.

Supplementary Figure 4 illustrates the measured electric-field intensity distributions and the corresponding fitted propagation lengths for the compound VPCs with $\delta w = 0.18$, 0.15, and 0.12, respectively. Supplementary Figures 4a to g show the electric-field intensity distributions of the topological valley QBICs in the compound VPC with $\delta w = 0.18$ from 0.497 THz to 0.512 THz, with a frequency increment of 0.0025 THz. The corresponding fitted propagation lengths are 1.88 mm, 1.73 mm, 1.84 mm, 2.57 mm, 4.64 mm, 7.04 mm, and 12.85 mm, respectively. Supplementary Figures 4h to n show the electric-field intensity distributions of the topological valley QBICs in the compound VPC with $\delta w = 0.15$ from 0.489 THz to 0.504 THz, with a frequency increment of 0.0025 THz. The corresponding fitted propagation lengths are 3.27 mm, 2.92 mm, 2.37 mm, 4.17 mm, 7.65 mm, 15.29 mm, and 17.66 mm, respectively. Supplementary Figures 4o to u show the electric-field intensity distributions of the topological valley QBICs in the compound VPC with $\delta w = 0.12$ from 0.485 THz to 0.500 THz, with a frequency increment of 0.0025 THz. The corresponding fitted propagation lengths are 3.34 mm, 3.50 mm, 7.41 mm, 11.79 mm, 18.28 mm, 7.08 mm, and 56.34 mm, respectively. In each lower panel, the red curves represent the extracted electric-field intensity profiles of the corresponding topological valley QBICs along the x-axis at $y = 0$ mm, while the black curve represents the exponential fitting used to determine the propagation length.

Supplementary Figure 5 illustrates the retrieved Q factors for the compound VPCs with δw = 0.18, 0.15, and 0.12, respectively. The differences between the experimentally retrieved and simulated Q factors may be caused by fabrication-induced additional radiative loss and variations in the fitted propagation length. The experimentally retrieved Q factors can be lower than the simulated values because residual side-etching and other fabrication imperfections may introduce additional scattering and radiative losses that are not fully captured in the idealized simulations. In contrast, when the experimentally retrieved Q factors are higher than the simulated values, the larger values may be associated with variations in the fitted propagation length caused by local field variations. Dust deposition during long-time scans, fabrication defects along the domain wall, and residual field fluctuations can locally modify the measured electric-field intensity profiles, thereby affecting the exponential fits and leading to an overestimation of the propagation length and Q factor.

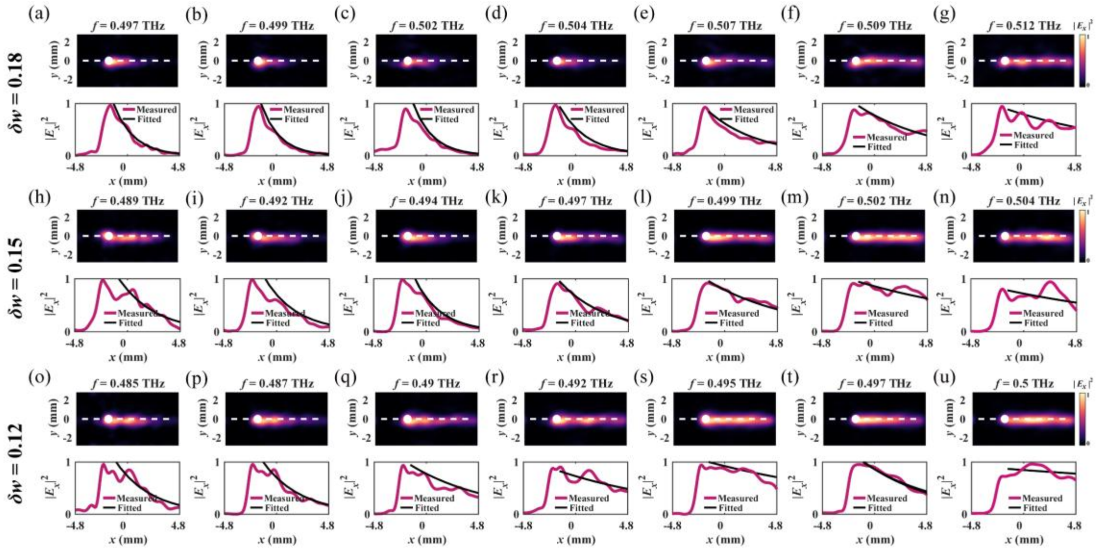

Supplementary Figure 4. The measured electric-field intensity distributions and fitted propagation lengths for the compound VPCs with δw = 0.18, 0.15, and 0.12, respectively. (a to g) The electric field intensity distributions of the topological valley QBICs in our compound VPCs with δw = 0.18 from 0.497 THz to 0.512 THz with an increment of 0.0025 THz, respectively. (h to n) The electric field intensity distributions of the topological valley QBICs in our compound VPCs with δw = 0.15 from 0.489 THz to 0.504 THz with an increment of 0.0025 THz, respectively. (o to u) The electric field intensity distributions of the topological valley QBICs in our compound VPCs with δw = 0.12 from 0.485 THz to 0.500 THz with an increment of 0.0025 THz, respectively. The red lines in the lower panels show the corresponding electric-field intensity distributions of the topological valley QBICs in the corresponding compound VPCs along the x-axis at y = 0 mm, respectively. The black lines in the lower panels show the corresponding exponential fits used to extract the propagation lengths.

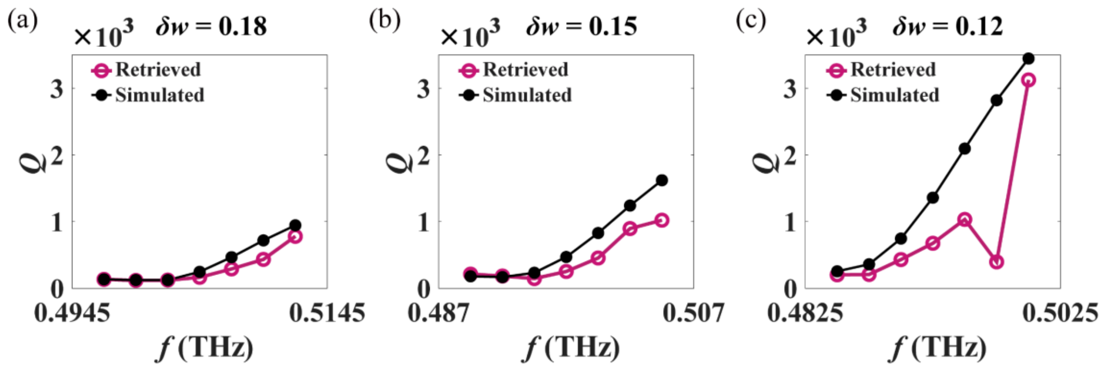

Supplementary Figure 5. The retrieved Q factors for the compound VPCs with δw = 0.18 (a), 0.15 (b), and 0.12 (c), respectively. The red circles and black dots represent the retrieved and simulated Q factors, respectively.

Supplementary Note 4. Robust transport

Near the folded Γ point, the opening of a small gap indicates the coupling between the K and K' valley components. Similar behavior has also been observed in valley-Hall-type systems, such as the Wu–Hu model in Ref. [S2], where a small gap can appear due to weak valley coupling while robust edge-state transport is still preserved.

In our system, by introducing small δw, the intervalley coupling remains weak away from the folded Γ point, such that valley polarization is largely preserved, and backscattering is strongly suppressed.

We performed a quantitative analysis of the valley composition using the experimentally measured near-field distributions. Specifically, we extracted the momentum-space field distributions through spatial Fourier transform of the measured complex near-field data and evaluated the spectral intensities around the folded K and K' valleys originating from the unmodulated VPC. We then define the valley-polarization contrast coefficient as $\eta = (I_K - I_{K'})/(I_K + I_{K'})$, where I_K and $I_{K'}$ are the integrated spectral intensities around the K and K' valleys, respectively. As shown in Supplementary Fig. 6, the extracted valley-polarization contrast coefficient remains high, with $\eta > 0.75$, for the compound VPC with δw = 0.12 at 0.490, 0.495, and 0.500 THz during propagation through the Z-bend domain wall. More importantly, the valley polarization before and after the bending region shows negligible redistribution between the K and K' components, indicating weak intervalley scattering during propagation. These results provide quantitative experimental evidence that the valley polarization of the edge states is largely retained despite the supercell modulation and Brillouin-zone folding.

Therefore, although finite valley mixing is introduced by the geometric modulation, robust valley-polarized transport is still experimentally preserved.

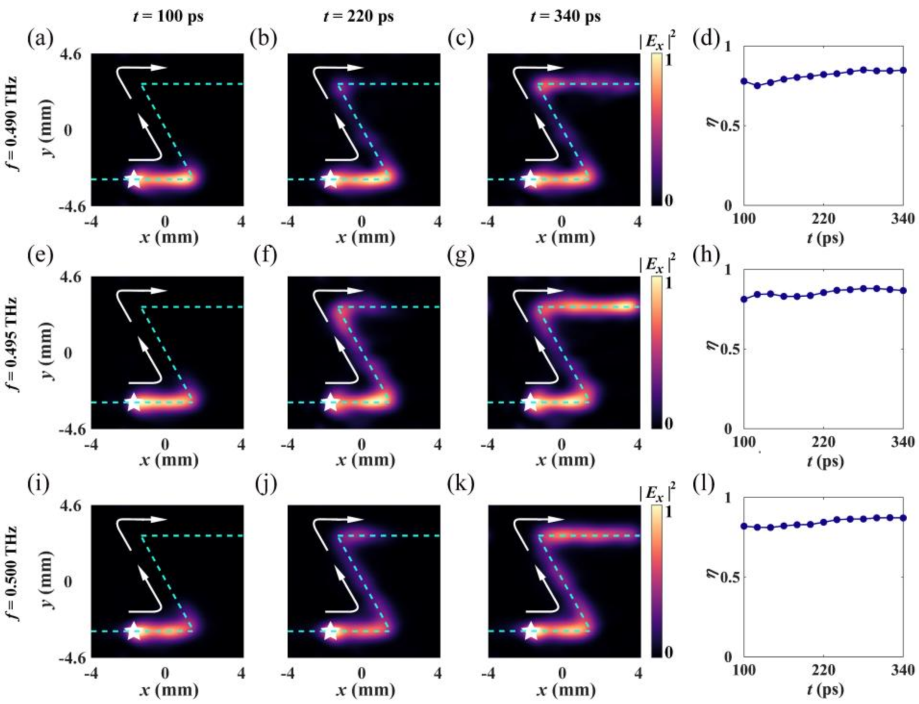

Supplementary Figure 6. Extracted measured electric-field intensity distributions and corresponding valley-polarization contrast coefficient η. (a to c) Extracted measured electric-field intensity distributions of the Z-bend domain wall with δw = 0.12 at 0.490 THz at different time delays during propagation. (d) Corresponding valley-polarization contrast coefficient η as a function of time delay. (e to g) Extracted measured electric-field intensity distributions of the Z-bend domain wall with δw = 0.12 at 0.495 THz at different time delays during propagation.

(h) Corresponding valley-polarization contrast coefficient η as a function of time delay. (i to k) Extracted measured electric-field intensity distributions of the Z-bend domain wall with δw = 0.12 at 0.500 THz at different time delays during propagation. (l) Corresponding valley-polarization contrast coefficient η as a function of time delay.

Supplementary Note 5. Normalized excitation coefficient of the valley QBIC modes
The absolute coupling efficiency from free-space waves to the valley QBIC modes is difficult to determine experimentally. It depends on the focused beam profile, excitation position, polarization state, and the fact that most of the mode energy is confined inside the silicon slab. The relative excitation strength of the valley QBIC can be quantified from the measured near-field data.

Specifically, we define a normalized excitation coefficient $\gamma(f) = \frac{|E_{\mathrm{QBIC}}(f)|^2}{\max(|E_{\mathrm{QBIC}}(f)|^2)}$, where $|E_{\mathrm{QBIC}}(f)|^2$ denotes the measured electric-field intensity of the valley QBIC mode at frequency (f). The coefficient γ serves as a normalized measure of the radiative accessibility of the valley QBICs. Supplementary Figure 7 shows the measured γ over a broad frequency range for compound VPCs with δw = 0.12, 0.15, and 0.18. The largest values of γ occur for valley QBICs located near the Γ point, where the radiative coupling to free-space waves is strongest. As the valley QBICs move away from the Γ point, the radiative accessibility gradually decreases, resulting in a reduced normalized coefficient.

To quantify the radiation bandwidth, we define it as the frequency range over which the normalized excitation coefficient γ remains above 50% of its peak value. The extracted bandwidths are 0.004 THz, 0.008 THz, and 0.015 THz for δw = 0.12, 0.15, and 0.18, respectively, at $k_xP = -0.11983\pi$ (Supplementary Figs. 7d to f). These results indicate that the radiation bandwidth increases with increasing δw, consistent with the enhanced radiative coupling and reduced Q factor of the corresponding valley QBICs.

As an example, a peak in γ is observed around 0.510 THz. When the operating frequency deviates from this resonance frequency, the normalized coefficient decreases rapidly because the frequency no longer matches that of the valley QBIC. Consequently, the excitation of the valley QBIC becomes weaker, leading to reduced transmitted signal intensity along the domain wall. For a sufficiently large frequency deviation, the valley QBIC can no longer be effectively excited.

We note that no peak is observed around 0.505 THz in Supplementary Fig. 7a. This may be due to imperfections in the Gaussian beam profile of the focused terahertz spot and the excitation position, which affect the excitation efficiency of the valley QBICs.

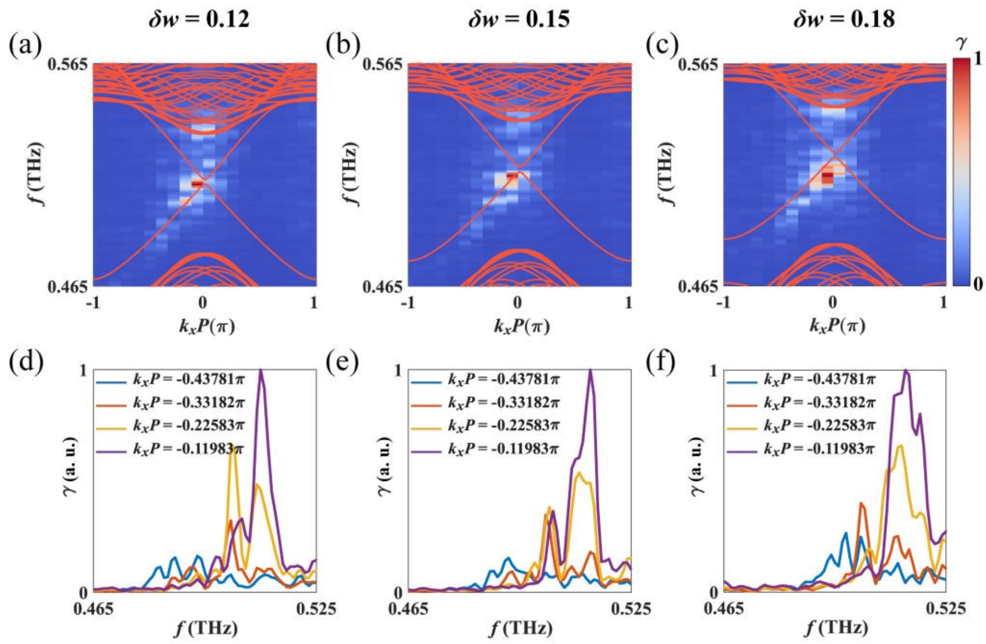

Supplementary Figure 7. Normalized coefficient γ for the compound VPCs. (a to c) Measured normalized coefficient γ for the compound VPCs with δw = 0.12, 0.15, and 0.18, respectively. The orange lines indicate the simulated projected dispersions of the domain wall formed by the corresponding compound VPCs. (d to f) Frequency-dependent normalized coefficient γ extracted at $k_xP = -0.11983\pi$, -0.22583π, -0.33182π and -0.43781π for the corresponding compound VPCs.

Supplementary Note 6. Band folding for bi-period, tri-period, and four-period

Similar QBIC functionality can also be achieved using bi-period and four-period structures through Brillouin-zone folding. The valley edge states of bi-period and four-period structures are also folded inside the light cone. Supplementary Figure 8 illustrates the dispersions of the bi-period, tri-period, and four-period structures. In general, a focused incident terahertz beam contains a distribution of in-plane momentum components, k_x, with most of its energy concentrated near the Γ point, $k_x = 0$. Therefore, modes folded closer to the Γ point can be more efficiently excited by free-space illumination than modes located at larger momenta.

Compared with the bi-period structure, the tri-period structure folds a larger portion of the valley edge-state dispersion toward the Γ point, resulting in more radiatively accessible modes within the momentum range covered by the focused terahertz beam.

Compared with the four-period structure, the tri-period structure exhibits a steeper dispersion around the accessible momentum range, corresponding to a larger group velocity and more efficient on-chip propagation.

Therefore, although both bi-period and four-period structures can support valley QBICs, the tri-period structure provides a more favorable balance among Brillouin-zone folding, radiative accessibility, momentum matching to free-space excitation, and on-chip propagation. This balance leads to more efficient excitation and transport of the valley QBICs, which is why the tri-period compound VPC was selected in our design.

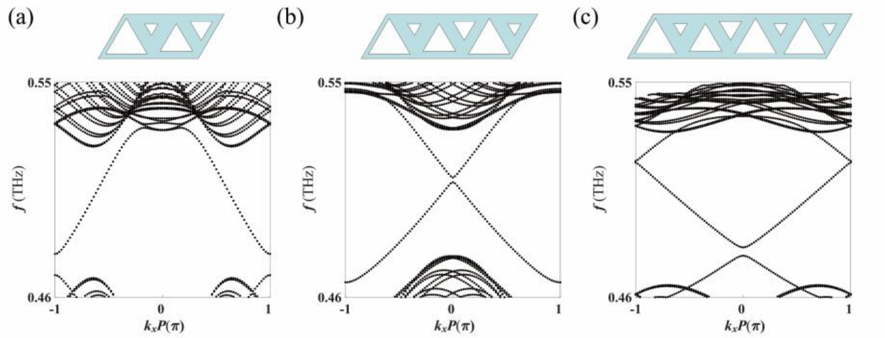

Supplementary Figure 8. Dispersions of the bi-period (a), tri-period (b), and four-period (c) structures, respectively.

Supplementary Note 7. The Type-A design in Ref. [S1]

In previous work, radiatively accessible terahertz valley states were demonstrated for on-chip-to-free-space radiation. In that design, the valley edge states were engineered to lie above the light cone, resulting in intrinsically leaky modes. Consequently, the valley edge states exhibit relatively low Q factors and short propagation lengths, which are advantageous for efficient out-coupling from the chip to free space and enable operation as a terahertz leaky-wave antenna.

To quantitatively compare the radiation characteristics, we performed additional simulations and experiments based on the Type-A design reported in Ref. [S1]. The Type-A structure consists of a VPC with a lattice constant of a = 300 μm and two triangular air holes with side lengths of 0.88a and 0.33a, respectively. In our fabricated samples, the silicon thickness was reduced from 220 μm to 150 μm, leading to an approximately 0.021 THz shift in the valley edge-state dispersion, as shown in Supplementary Figs. 9a and b. The simulated Q factor changes from approximately 85.94 to 70.41, confirming that the structure remains in a strongly radiative regime.

As shown in Supplementary Figs. 9d to f, the simulated electric-field distributions at 0.33, 0.34, and 0.35 THz show rapid radiation away from the waveguide, consistent with the design principle of a leaky-wave antenna. The corresponding propagation lengths are extracted from exponential fitting of the electric-field intensity profiles using $|E(x)|^2 \propto \exp(-x/L)$, where x and L denote the coordinate and the characteristic propagation length, respectively. The extracted simulated propagation lengths are 0.61 mm, 1.94 mm, and 3.70 mm, respectively. The experimentally measured propagation lengths are 0.64 mm, 1.16 mm, and 2.82 mm, as illustrated in Supplementary Figs. 9g to i, respectively. The slight discrepancies are attributed to experimental noise, finite signal-to-noise ratio, and fluctuations in the measured near-field intensity profiles.

Overall, these results indicate that the Type-A valley edge states operate in a strongly radiative leaky-wave regime with comparatively short propagation lengths, which is suitable for free-space radiation but less suitable for long-distance on-chip valley transport. In contrast, our work aims to achieve free-space accessibility while preserving robust on-chip transport through Brillouin-zone-folding-induced valley QBICs. This mechanism introduces a controllable radiative channel through a weak periodic geometric perturbation, enabling a tunable balance between free-space coupling and low-loss topological propagation.

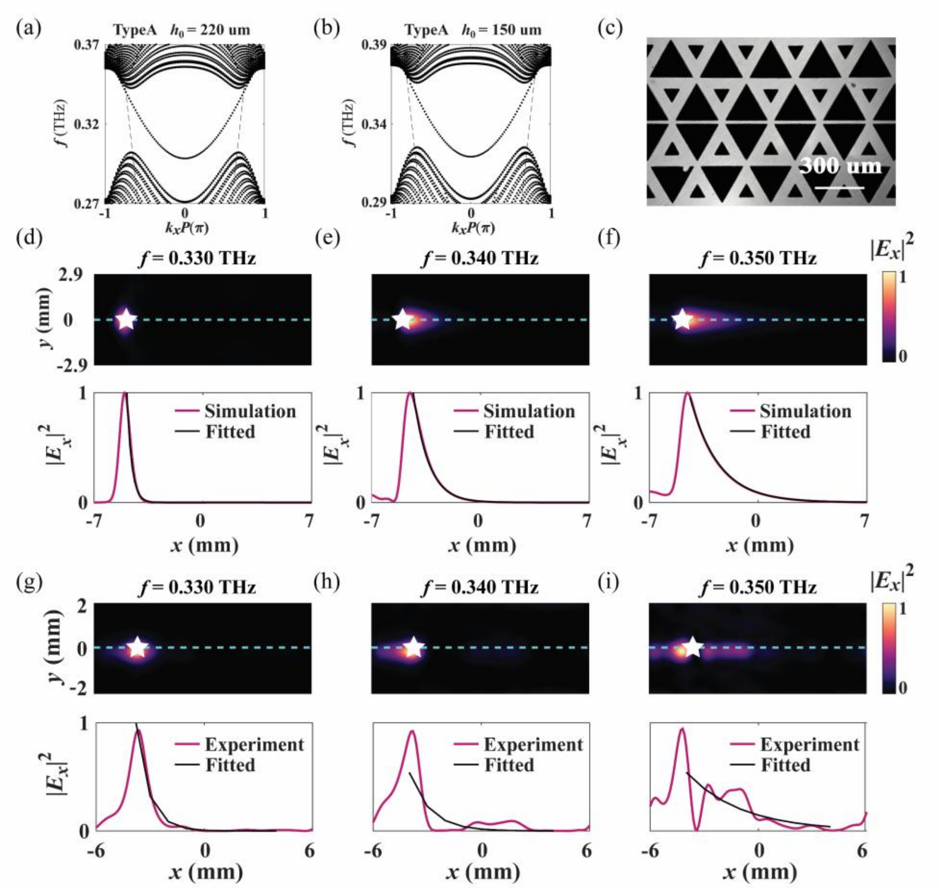

Supplementary Figure 9. The simulated and measured results of the Type-A design. (a and b) The simulated dispersions of the Type-A design with the thicknesses of 220 μm and 150 μm, respectively. (c) The optical image of the fabricated Type-A sample with a thickness of 150 μm. (d to f) The simulated electric-field intensity distributions of the Type-A design's valley edge states at 0.33 THz, 0.34 THz, and 0.35 THz, respectively. The lower panels show the corresponding electric-field intensity distributions of the Type-A valley edge states along the x-axis at y = 0 mm, respectively. The black lines show the corresponding exponential fits used to extract the propagation lengths. (g to i) The corresponding measured electric field intensity distributions of the Type-A design. The lower panels show the corresponding electric-field intensity distributions of the Type-A valley edge states along the x-axis at y = 0 mm, respectively. The black lines show the corresponding exponential fits used to extract the propagation lengths. The electric field intensity distributions are normalized by the maximum absolute value of the electric field intensities in the corresponding figures.

Supplementary Note 8. Dispersion of the domain wall along $\boldsymbol{d} = (-1/2, \sqrt{3}/2)$ direction

We consider a bent domain wall oriented along $\boldsymbol{d} = (-1/2, \sqrt{3}/2)$ direction in our coordinate convention. In our work, a supercell modulation with period P is introduced along the x-direction, as shown in Supplementary Fig. 10a. The lattice vectors change from $\boldsymbol{a}_{VPC,1} = (1,0)P/3$, $\boldsymbol{a}_{VPC,2} = (-1/2, \sqrt{3}/2)P/3$ (VPC) for the unmodulated VPC to $\boldsymbol{a}_1 = (1,0)P$, $\boldsymbol{a}_2 = (-1/2, \sqrt{3}/2)P/3$ for the compound VPC, respectively. The corresponding reciprocal lattice vectors change from $\boldsymbol{b}_{VPC,1} = (\frac{6\pi}{P}, \frac{6\pi}{\sqrt{3}P})$, $\boldsymbol{b}_{VPC,2} = (0, \frac{12\pi}{\sqrt{3}P})$ (VPC) for the unmodulated VPC to $\boldsymbol{b}_1 = (\frac{2\pi}{P}, \frac{2\pi}{\sqrt{3}P})$, $\boldsymbol{b}_2 = (0, \frac{12\pi}{\sqrt{3}P})$ for the compound VPC, respectively. Therefore, the Brillouin-zone boundary associated with $\boldsymbol{b}_1$ is folded, whereas the boundary associated with $\boldsymbol{b}_2$ remains unchanged.

According to the relation between the lattice vectors and reciprocal lattice vectors $\boldsymbol{a}_i \cdot \boldsymbol{b}_j = 2\pi\delta_{ij}$, we obtain $\boldsymbol{a}_2 \cdot \boldsymbol{b}_1 = 0$ and $\boldsymbol{a}_2 \cdot \boldsymbol{b}_2 = 2\pi$. Since the vector $\boldsymbol{d}$ is parallel to $\boldsymbol{a}_{VPC,2}$ and $\boldsymbol{a}_2$, the unchanged lattice vector $\boldsymbol{a}_2$ and reciprocal vector $\boldsymbol{b}_2$ determine the Brillouin-zone boundary relevant to edge states propagating along the ***d***-direction. Therefore, the projected Brillouin-zone boundary along the ***d***-direction remains unchanged, as shown in Supplementary Fig. 10b, and no Brillouin-zone folding occurs in the corresponding edge-state dispersion shown in Supplementary Fig. 10c.

Consequently, introducing geometric modulation in one lattice vector direction does not universally induce Brillouin-zone folding for all lattice vector directions.

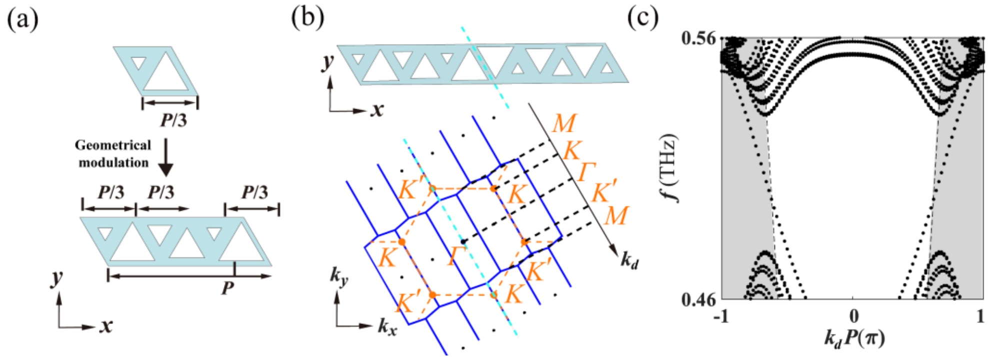

Supplementary Figure 10. A modulated VPC with a domain wall along the $\boldsymbol{d} = (-1/2, \sqrt{3}/2)$ direction. (a) Schematic of the unit cell with geometric modulation introduced along the x-direction. (b) Corresponding two-dimensional Brillouin zone and projected domain-wall direction along $\boldsymbol{d} = (-1/2, \sqrt{3}/2)$ direction. (c) Dispersion of the domain wall in (b). The gray shaded region indicates the light cone.

References

S1 Wang, W. et al. On-chip topological leaky-wave antenna for full-space terahertz wireless connectivity. *Nat. Photon.* **20**, 317–323 (2026).

S2 Wu, L. & Hu, X. Scheme for Achieving a Topological Photonic Crystal by Using Dielectric Material. *Phys. Rev. Lett.* **114**, 223901 (2015).